BIOCHEMISTRY
including biophysical chemistry & molecular biology

Article

pubs.acs.org/biochemistry

Redox Potential Tuning through Differential Quinone Binding in the Photosynthetic Reaction Center of *Rhodobacter sphaeroides*

Josh V. Vermaas,[†,‡,§] Alexander T. Taguchi,[†,∥,‡,@] Sergei A. Dikanov,[∥] Colin A. Wraight,[⊥,†,‡] and Emad Tajkhorshid*[,†,‡,§]

[†]Center for Biophysics and Computational Biology, [‡]Department of Biochemistry, [§]Beckman Institute, and [∥]Department of Veterinary Clinical Medicine, University of Illinois at Urbana-Champaign, Urbana, Illinois 61801, United States

Supporting Information

ABSTRACT: Ubiquinone forms an integral part of the electron transport chain in cellular respiration and photosynthesis across a vast number of organisms. Prior experimental results have shown that the photosynthetic reaction center (RC) from *Rhodobacter sphaeroides* is only fully functional with a limited set of methoxy-bearing quinones, suggesting that specific interactions with this substituent are required to drive electron transport and the formation of quinol. The nature of these interactions has yet to be determined. Through parameterization of a CHARMM-compatible quinone force field and subsequent molecular dynamics simulations of the quinone-bound RC, we have investigated and characterized the interactions of the protein with the quinones in the Q_A and Q_B sites using both equilibrium simulation and thermodynamic integration. In particular, we identify a specific interaction between the 2-methoxy group of ubiquinone in the Q_B site and the amide nitrogen of GlyL225 that we implicate in locking the orientation of the 2-methoxy group, thereby tuning the redox potential difference between the quinones occupying the Q_A and Q_B sites. Disruption of this interaction leads to weaker binding in a ubiquinone analogue that lacks a 2-methoxy group, a finding supported by reverse electron transfer electron paramagnetic resonance experiments of the $Q_A^-Q_B^-$ biradical and competitive binding assays.

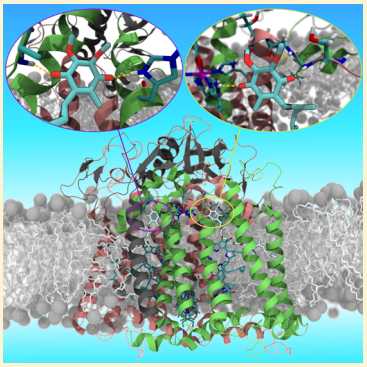

The reaction center (RC) of the photosynthetic bacteria *Rhodobacter sphaeroides* is a model system for studying type II photosynthetic RCs. Its role in the photoreduction of quinone to quinol has been extensively studied[1,2] and well-established (Figure 1). In brief, light excitation of a bacteriochlorophyll dimer results in electron transfer through the A branch bacteriochlorophyll and bacteriopheophytin monomers to the Q_A site (arrow from P to Q_A in Figure 1). The resulting anionic semiquinone, Q_A^-, exploits the 60−80 mV[3,4] redox potential difference between Q_A and the secondary quinone (Q_B) such that inter-quinone electron transport (the arrow between Q_A and Q_B in Figure 1) results in a new charge-separated state, $P^+Q_B^-$. A second light excitation of the RC further reduces the semiquinone in Q_B to quinol by means of a proton-coupled electron transfer reaction. The weakly bound quinol then dissociates from the RC and shuttles its electrons to the bc_1 complex, forming the basis for bacterial photosynthesis.

The origins of the redox potential difference between the Q_A and Q_B sites necessary for inter-quinone electron transfer are unclear. Unlike in *Rhodopseudomonas viridis*, where the RC is believed to exploit the inherent redox potential difference[5] of chemically distinct quinones,[6,7] the Q_A and Q_B sites of *R. sphaeroides* RC are occupied by identical quinone molecules, UbiQ-10 (ubiquinone-10, whose quinone head is 2,3-dimethoxy-5-methyl-6-isoprenyl-1,4-benzoquinone). This suggests that the RC, through different interactions with the two quinones, tunes the redox potentials of the individual UbiQ molecules. Previous density functional theory−electron paramagnetic resonance (EPR) experiments have concluded that different orientations of the 2-methoxy group [but not the 3-methoxy group (Figure 2)] in Q_A and Q_B are responsible for establishing the functional quinone redox potential difference.[8−10]

Quinones that lack these methoxy groups, such as plastoquinone (2,3-dimethyl-6-isoprenyl-1,4-benzoquinone), are nonfunctional in the *Rhodobacter* RC.[11] Through the use of synthetic quinones in which one of the two methoxy groups of UbiQ is replaced by a methyl, creating a monomethoxy quinone [MMQ (Figure 2C)], it has been shown that inter-quinone electron transfer takes place only when the Q_B site is occupied by a quinone that bears a 2-methoxy group, such as 2-monomethoxy ubiquinone (2MeO-Q, 2-methoxy-3,5-dimethyl-6-isoprenyl-1,4-benzoquinone) that lacks a 3-methoxy group.[12] In the absence of the 2-methoxy group, e.g., when 3-monomethoxy ubiquinone (3MeO-Q, 3-methoxy-2,5-dimethyl-6-isoprenyl-1,4-benzoquinone) is bound to the RC, only formation of a Q_A radical upon light excitation is observed, as opposed to the case of 2MeO-Q where both Q_A and Q_B are functional.[12] As removal of either methoxy group did not

Received: January 13, 2015
Revised: March 2, 2015
Published: March 3, 2015

DOI: 10.1021/acs.biochem.5b00033
Biochemistry 2015, 54, 2104−2116

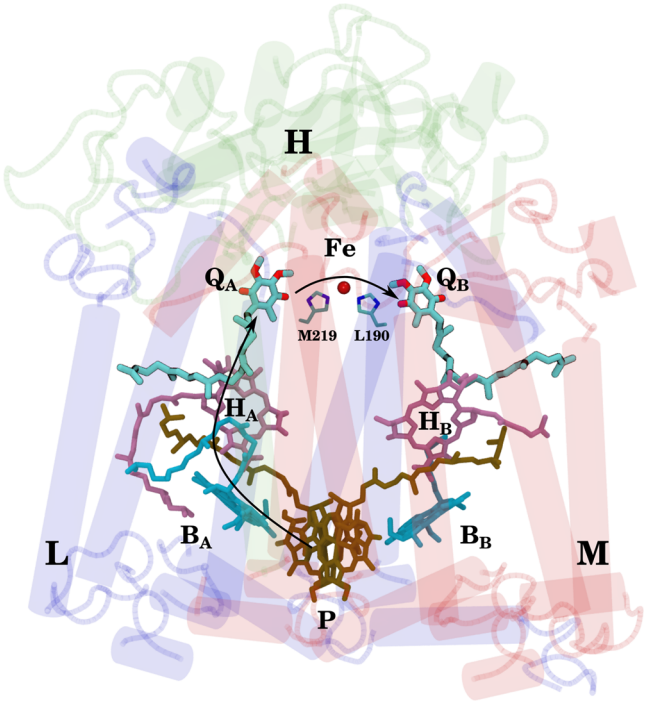

Figure 1. Electron transport pathway within the reaction center (RC) of *R. sphaeroides*. The three subunits of the RC are labeled (green for H, blue for L, and red for M), along with their associated cofactors (ubiquinones Q_A and Q_B, primary donor P, and bacteriochlorophylls B_A, B_B, H_A, and H_B), as well as important residues for inter-quinone electron transfer, namely, a pair of histidines (HisM219 and HisL190) and a non-heme iron. Electrons travel along the A branch from P to Q_A, and across the non-heme iron from Q_A to Q_B, as indicated by the black arrows.

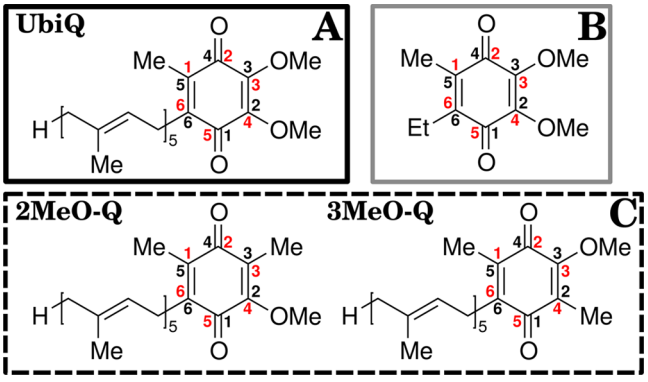

Figure 2. Relevant chemical structures. (A) Ubiquinone (UbiQ) is bordered with a solid black outline, while the monomethoxy quinones (MMQ) 2MeO-Q (2-monomethoxy ubiquinone) and 3MeO-Q (3-monomethoxy ubiquinone) are collectively bordered by a dotted black outline (C). (B) The molecule used for parameterization of UbiQ, 2,3-dimethoxy-5-methyl-6-ethyl-1,4-benzoquinone, is outlined in gray. Similar compounds were used for the parameterization of 2MeO-Q and 3MeO-Q (not shown). The alternative numbering schemes for the quinone ring are also labeled. In bold black font is the conventional carbon numbering scheme used to refer to individual atoms throughout the text, while the red numbers follow the crystallographic naming convention for UbiQ-10 and were used when generating the topology and parameter files for the simulation.

impair or substantially alter Q_A activity, the loss of methoxy specific interactions in the Q_B site seems to be responsible for the observed inactivity of 3MeO-Q in the RC. On the basis of EPR and MMQ activity assays,[9,12] the effects of the 2-methoxy group on the affinity of UbiQ and the tuning of the redox potential of the Q_B site have been previously proposed to underlie the observed phenomenon, although the nature of the interactions has not been elucidated.

Molecular dynamics (MD) simulations offer the simultaneous spatial (angstrom) and temporal (femtosecond) resolution needed to characterize the specific interactions between the quinones in the Q_A and Q_B sites. Through equilibrium MD simulations, we have identified different hydrogen bonding patterns between the quinones occupying the respective Q_A and Q_B sites, which have been elusive in prior experimental studies. In addition, MD permits the calculation of experimental observables, such as binding affinities through thermodynamic integration (TI), that can be connected back to experiment. In parallel, we have also conducted EPR experiments in which a $Q_A^{\bullet-}Q_B^{\bullet-}$ biradical is formed by reverse electron transfer from Q_B^{2-} to Q_A and relative binding assay measurements that specifically address the activity and binding of 3MeO-Q to the Q_B site.

A prerequisite for any classical MD simulation is an empirical force field to describe the atomic interactions. UbiQ parameters already exist in AMBER[13] and CHARMM;[14,15] however, no parameters have been developed for 2MeO-Q or 3MeO-Q, and existing parameters for CHARMM do not describe methoxy dihedral rotation. Differences between the parameterization procedures for different force fields can result in different structural features, such as protein secondary structure formation,[16] so the existing AMBER parameters should not be used within a CHARMM36 simulation. To generate CHARMM-compatible parameters, we follow conventional CHARMM parameterization methodology[17] through the use of *ff*TK (Force Field Toolkit)[18] to develop a consistent set of parameters for UbiQ and its two MMQ derivatives.

Building upon these new parameters, we have run both equilibrium simulations and TI calculations to investigate protein−quinone interactions in the Q_A and Q_B sites and how these interactions influence methoxy dihedral orientation and monomethoxy binding within the RC. We identify specific protein−quinone interactions, including a hydrogen bond between the backbone of GlyL225 and the 2-methoxy oxygen in the Q_B site, that serve to break the symmetry between the Q_A and Q_B sites and drive electron transfer. The TI calculations suggest that 3MeO-Q has a binding affinity lower than that of 2MeO-Q or UbiQ in the Q_B site, which is supported by our experimental measurements. In contrast, no difference in affinity between either MMQ and UbiQ is observed in the Q_A site. On the basis of these results, we propose that the GlyL225 hydrogen bond with the 2-methoxy group stabilizes UbiQ in the Q_B site and is responsible for holding the 2-methoxy dihedral angle into its out-of-plane orientation necessary to establish the 60−80 mV functional redox potential difference between Q_A and Q_B.[3,4]

METHODS

To accomplish our research objectives, we adopted a concerted computational and experimental approach. Determination of 2MeO-Q and 3MeO-Q binding was conducted both by TI calculations that yield relative binding affinities and by competitive binding assays and EPR experiments with the $Q_A^{\bullet-}Q_B^{\bullet-}$ biradical that focus on the interactions of the 2-methoxy group. Thus, while we present the methodology separately, there is a tight connection between computational and

DOI: 10.1021/acs.biochem.5b00033
Biochemistry 2015, 54, 2104−2116

experimental studies, and where possible, we connect back-calculated quantities to experimental observables. There are two different commonly used numbering schemes for atomic positions in UbiQ (Figure 2). Crystallographers consider C1 to be the carbon adjacent to the isoprene tail farthest from the methoxy groups in U10 [the residue name for UbiQ-10 in the Protein Data Bank (PDB)], while IUPAC considers C1 to be the carbonyl carbon adjacent to the tail (Figure 2). To be consistent with the nomenclature in the PDB, in setting up the topology file for the quinones and in other simulation files, we followed crystallographic numbering. However, in discussing the results, we follow IUPAC nomenclature to maintain consistency with prior studies with MMQs[8,12] and the wider literature on quinone chemistry.

Computational Methods. The starting point for all simulations was the structure of the bacterial RC (PDB entry 1DV3),[19] which was chosen because of its planar UbiQ structure in the Q_B site when compared to later structures with comparable resolution.[20] The planar structure suggests that the crystallographic quinone is closer to its equilibrium position, reducing the impact of applied constraints during the initial equilibration phase. The 1DV3 structure contains five resolved isoprene units; thus, all simulations conducted use a quinone head with a five-isoprene tail. The isoprenoid tail of UbiQ is membrane-exposed when bound to the RC complex. To better represent this in the simulation system, the complex was embedded in a 90 Å × 100 Å 1-palmitoyl-2-oleoylphosphatidylcholine (POPC) membrane and solvated such that the axis parallel to the membrane normal was 115 Å long with a NaCl concentration in solution of 150 mM (Figure S1 of the Supporting Information). The simulations were conducted with NAMD 2.9,[21] using the CHARMM36 force field for proteins[22−24] and lipids,[25] the TIP3P water model,[26] and existing parameters for cofactors excluding the quinones.[14,27] UbiQ, 2MeO-Q, and 3MeO-Q were reparameterized for CHARMM using *ff*TK,[18] with a detailed description of the methodology in the following section.

Parameters shared by all the simulations include the nonbonded cutoffs, with a real space cutoff of 12 Å (switching after 10 Å), the inclusion of long-range electrostatics through the use of the particle mesh Ewald (PME) method[28,29] with a 1 Å grid spacing, and 2 fs time steps and the requisite use of SETTLE[30] to constrain bond lengths to hydrogen atoms. All simulations were performed at a constant temperature (310 K unless specified otherwise) and pressure (1 atm), maintained by Langevin dynamics and Langevin piston Nosé−Hoover methods, respectively.[31,32]

Parameterization of UbiQ and Monomethoxy Derivatives. Given the ubiquitous nature of UbiQ, molecular mechanics parameter sets have been developed to model its behavior, most notably existing parameter sets for AMBER[13] and CHARMM.[14,15] The AMBER parameters are incompatible with the CHARMM force field because of their differing methodologies for computing parameters for electrostatic and nonbonded interactions, which in turn also result in differences in the bonded parameters. The prior CHARMM parameter sets for UbiQ were not obtained in a manner consistent with the rest of the force field and, unfortunately for our purposes, did not model force constants for the dihedral torsions. Because we are studying interactions that contribute to the orientation of the methoxy group, thereby tuning the redox potential, it was necessary to reparameterize UbiQ. As we were most concerned with the behavior of the quinone ring itself, parameters for the isoprene tails were taken by analogy from the lipid force field.[25]

The reparameterization was conducted within the framework provided by *ff*TK,[18] a recently developed plugin within VMD[33] that streamlines the preparation and analysis of quantum mechanical target data to generate CHARMM-compatible parameters in a manner consistent with the CHARMM General Force Field (CGenFF).[17] The two model compounds used for full parameterization were 2,3-dimethoxy-5-methyl-6-ethyl-1,4-benzoquinone (Figure 2B) and 2-methoxy-3,5-dimethyl-6-ethyl-1,4-benzoquinone, which are truncated versions of UbiQ and 2MeO-Q, respectively (Figure 2A,C), with the 6-ethyl representing a truncated isoprene group, analogous to the case in prior studies focused on methoxy dihedral behavior.[34] As the atomic partial charges are sensitive to the position of substituents on the ring, the corresponding truncated version of 3MeO-Q was subjected to the charge optimization step to arrive at an independent charge distribution. However, as the dihedral terms are identical to those found in 2MeO-Q, 3MeO-Q uses 2MeO-Q bond, angle, and dihedral parameters. The parameterization process follows standard CHARMM force field parameter development[17,18,35] and is detailed in the Supporting Information.

The final parameter set is provided in the Supporting Information; however, the form of the dihedral terms used to describe the rotation about the methoxy−oxygen−ring bond requires additional discussion. In existing X-ray structures, the methoxy methyl groups are oriented out of the quinone ring plane in both Q_A and Q_B[36−39] by differing degrees, suggesting that those are the stable conformations in the protein environment. This geometry in UbiQ is in part a steric effect, as suggested by prior computational studies of UbiQ and analogues[40,41] and observed resonances with IR spectroscopy.[42] However, when the methoxy is in plane, the methoxy oxygen is conjugated into the benzoquinone π-system, lowering the overall energy and redistributing charges (Figure S2 of the Supporting Information). Thus, the QM-optimized geometries in vacuum for 2MeO-Q and 3MeO-Q have the methoxy methyl in plane with the quinone ring pointed away from the nearest carbonyl. The minimal energy configuration found for UbiQ (2,3-dimethoxy-5-methyl-6-ethyl-1,4-benzoquinone) has one methoxy in the quinone plane in a geometry similar to that of MMQ and the other methoxy out of plane. The final parameter set treats the minimal energy conformation for the dihedral term as bringing both methoxys in plane, with the minimal values for the dihedral at 0° and 180° and a periodicity of 2, counter to the observed methoxy orientations in crystallographic structures. Thus, any out-of-plane motion will be a result of nonbonded interactions within the quinone.

To assess the performance of the parameters, we calculate the solvation free energy at 296 K for Q0 (2,3-dimethoxy-5-methyl-1,4-benzoquinone), Q0M (2,3-dimethoxy-5,6-dimethyl-1,4-benzoquinone), and Q1 (2,3-dimethoxy-5-methyl-6-isoprenyl-1,4-benzoquinone) in water, octanol, hexane, and cyclohexane using free energy perturbation (FEP)[43] to compare against experimentally determined partition coefficients.[44] The FEP details are given in the Supporting Information. The analysis of the FEP simulations was conducted using the ParseFEP plugin[45] of VMD,[33] with the reported uncertainties calculated using the Bennett acceptance ratio.[46] Parameters for octanol, hexane, and cyclohexane were taken from CGenFF.[17]

Equilibrium Simulations of Membrane-Embedded Reaction Centers. Three sets of 300 ns equilibrium simulations were

DOI: 10.1021/acs.biochem.5b00033
Biochemistry 2015, 54, 2104−2116

conducted, each with a different quinone (UbiQ, 2MeO-Q, and 3MeO-Q) occupying both the Q_A and Q_B sites, with the equilibration process described in the Supporting Information. One additional 100 ns simulation was conducted with UbiQ in the Q_A and Q_B sites, where AspL213 was protonated to investigate the consequences for the hydrogen bonding of SerL223. Analysis of the resulting trajectories was conducted in VMD,[33] using features including the HBONDS plugin, as well as its scripting capabilities to measure specific dihedrals and distances and to visualize neighboring interactions. Plots were generated using Matplotlib.[47]

Thermodynamic Integration (TI) Calculations. TI calculations[48−50] were set up to determine the binding affinity for 2MeO-Q and 3MeO-Q relative to UbiQ in the Q_A and Q_B sites through the use of thermodynamic cycles to transition between states. The state definitions and transition nomenclature are detailed in Figure 3. Two binding affinity changes were calculated, one of which used the quinone in aqueous solution as the reference ($\Delta\Delta G^{s\rightarrow p}_{\mathrm{UbiQ}\rightarrow\mathrm{MMQ}}$), and another using a membrane-exposed quinone with the headgroup located at a bilayer interface ($\Delta\Delta G^{m\rightarrow p}_{\mathrm{UbiQ}\rightarrow\mathrm{MMQ}}$). This entails four alchemical transitions per MMQ derivative (eight total). Two alchemical transitions calculate the UbiQ to MMQ transition within the Q_A and Q_B sites of the RC ($\Delta G^{p}_{\mathrm{UbiQ}\rightarrow\mathrm{MMQ}}$). The other two alchemical transitions calculate the UbiQ to MMQ transition in solution ($\Delta G^{s}_{\mathrm{UbiQ}\rightarrow\mathrm{MMQ}}$) and membrane ($\Delta G^{s}_{\mathrm{UbiQ}\rightarrow\mathrm{MMQ}}$). The transitions within the RC used the membrane-embedded RC from the equilibrium trajectories as the starting point. Transitions between UbiQ and MMQ in aqueous solution were conducted in a water cube with 40 Å sides. Membrane transitions were conducted in a solvated 1-palmitoyl-2-oleoylphosphatidylethanolamine (POPE) membrane, with 40 Å sides perpendicular to the membrane normal and a 60 Å length parallel to it.

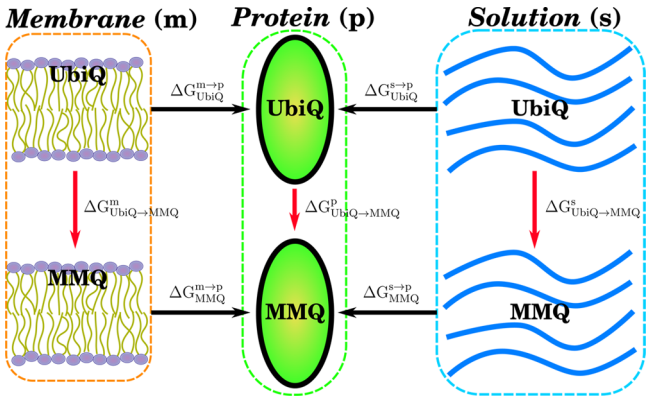

Figure 3. Schematic of the states connected using thermodynamic integration. Ubiquinone (UbiQ) is the quinone present in the top states, while one of the monomethoxy quinones (MMQ), either 2MeO-Q or 3MeO-Q, is present below. The quinone is either immersed in a lipid bilayer (left, denoted m for membrane), the Q_A or Q_B site of the RC (middle, denoted p for protein), or immersed in water (right, denoted s for solution). Horizontal black arrows are used to denote state transitions that are accessible in nature, while vertical red arrows denote alchemical state transitions performed *in silico*. Because the free energy change around a closed loop must be zero, we can connect the alchemical state transitions to relative binding free energies. Specifically, $\Delta G^{m\rightarrow p}_{\mathrm{MMQ}} - \Delta G^{m\rightarrow p}_{\mathrm{UbiQ}} = \Delta G^{p}_{\mathrm{UbiQ}\rightarrow\mathrm{MMQ}} - \Delta G^{m}_{\mathrm{UbiQ}\rightarrow\mathrm{MMQ}} = \Delta\Delta G^{m\rightarrow p}_{\mathrm{UbiQ}\rightarrow\mathrm{MMQ}}$, and $\Delta G^{s\rightarrow p}_{\mathrm{MMQ}} - \Delta G^{s\rightarrow p}_{\mathrm{UbiQ}} = \Delta G^{p}_{\mathrm{UbiQ}\rightarrow\mathrm{MMQ}} - \Delta G^{s}_{\mathrm{UbiQ}\rightarrow\mathrm{MMQ}} = \Delta\Delta G^{s\rightarrow p}_{\mathrm{UbiQ}\rightarrow\mathrm{MMQ}}$. In addition, we can also compute the relative free energy change for membrane partitioning between MMQ and UbiQ by connecting the left and right states directly via $\Delta G^{s\rightarrow m}_{\mathrm{MMQ}} - \Delta G^{s\rightarrow m}_{\mathrm{UbiQ}} = \Delta G^{m}_{\mathrm{UbiQ}\rightarrow\mathrm{MMQ}} - \Delta G^{s}_{\mathrm{UbiQ}\rightarrow\mathrm{MMQ}} = \Delta\Delta G^{s\rightarrow m}_{\mathrm{UbiQ}\rightarrow\mathrm{MMQ}}$.

The TI reaction coordinate is described in the Supporting Information and featured a 20 kcal mol^{-1} $\mathrm{Å}^{-2}$ harmonic potential applied between heavy atoms in the MMQ rings to their corresponding partner in UbiQ to eliminate sampling unphysical conformations that can result in the slow convergence of the TI calculations.[51,52] The results when such restraints are not applied are detailed in the Supporting Information. The free energy integration itself was conducted on a third-order penalized spline (P-spline[53]) fit of the average $dU/d\lambda$ over 5 ns (10 ns for solution) of simulation time. Before the production simulations, each window was equilibrated for 0.5 ns where collected data did not contribute to the average. Statistical error estimates were obtained using a methodology detailed by Steinbrecher et al.[54]

Experimental Methods. RCs used in this study were isolated from a strain of *R. sphaeroides* expressing the protein with a histidine tag on the M subunit.[55] The quinones were extracted by the method of Okamura et al.[56] and replaced with 2MeO-Q, 3MeO-Q, or UbiQ with a four-isoprene tail (UbiQ-4) where appropriate. The synthetic quinones have isoprenoid tails shorter than what was simulated (four units rather than five). Occasionally, a native UbiQ (with all 10 isoprene units present, UbiQ-10) was used as a reference point, which is clearly indicated.

Previous studies showed that RCs reconstituted with 3MeO-Q were incapable of electron transfer from Q_A^- to Q_B, preventing the formation of a 3MeO-Q Q_B^- radical.[12] This has hindered EPR-based investigation of the interaction of 3MeO-Q in Q_B. However, while the quinone redox potential difference is unfavorable for forward electron transfer, the loss of the 2-methoxy group in 3MeO-Q is expected to facilitate the reverse reaction $Q_AQ_B^- \rightleftarrows Q_A^-Q_B$.[8] When the quinone pool is fully reduced to quinol, an equilibrium is established between the EPR silent state Q_B^{2-} and the EPR active state $Q_A^-Q_B^-$ via electron disproportionation.[57] Above pH 8.5, this equilibrium favors formation of the $Q_A^-Q_B^-$ biradical. This reverse electron transfer reaction is very likely to also occur for 3MeO-Q-bound RCs, because the one-electron redox potential for this quinone analog is higher for Q_A than for Q_B.[9]

In this experiment, the quinone pool was reduced and the pH adjusted by the method of Calvo et al.[57] The high-spin Fe^{2+} was removed from the RC by biochemically replacing Fe^{2+} with diamagnetic Zn^{2+} according to the procedures outlined by Utschig et al.[58] to remove the broad signal arising from the coupling of the semiquinone to the high-spin Fe^{2+}. EPR samples were generated by borohydride ($NaBH_4$) reduction at pH 10.5 in a D_2O buffer to reduce the EPR line width. All continuous wave (CW) Q-band measurements were performed on a Bruker ELEXSYS E580 EPR spectrometer equipped with an Oxford CF 935 cryostat and an ER 5106 QT resonator.

Kinetic measurements were performed on a spectrometer of local design, capable of delivering an actinic flash to the RC sample, and monitoring the subsequent kinetics to establish the rate constants for the decay of the charge-separated state:

$$\begin{tikzcd} \mathrm{PQ_AQ_B} \arrow[r, shift left, "h\nu"] & \mathrm{P^+Q_A^-Q_B} \arrow[l, shift left, "\mathrm{k_{AP}}"] \arrow[r, leftrightarrow, "\mathrm{K_{AB}}"] & \mathrm{P^+Q_AQ_B^-} \arrow[ll, bend left, "\mathrm{k_{BP}}"] \end{tikzcd}$$

Table 1. Calculated Solvation Free Energies (in kilocalories per mole) for the Newly Parameterized UbiQ with Varying Tail Lengths, Along with the Resulting Log P Values, Compared to Experimental Values[44,a]

	water	octanol			cyclohexane			hexane	
	ΔG_{solv}	ΔG_{solv}	log P	exp. log P[44]	ΔG_{solv}	log P	exp. log P[44]	ΔG_{solv}	log P
Q0	−5.3 ± 0.4	−6.12 ± 0.07	0.63 ± 0.28	0.78	−3.89 ± 0.06	−1.02 ± 0.28	0.39	−3.85 ± 0.05	−1.05 ± 0.28
Q0M	−4.77 ± 0.25	−6.66 ± 0.08	1.40 ± 0.19	1.26	−5.01 ± 0.06	0.18 ± 0.19	0.73	−4.86 ± 0.06	0.07 ± 0.19
Q1	−4.11 ± 0.26	−9.28 ± 0.09	3.82 ± 0.20	>3	−8.19 ± 0.07	3.01 ± 0.19	>3	−7.66 ± 0.07	2.62 ± 0.19

[a]The relationship between log P and the computed solvation free energies is $\log P_X = -(\Delta G^X_{solv} - \Delta G^{water}_{solv})/RT \ln 10$. The quinones are referenced by their abbreviations. Q0 is 2,3-dimethoxy-5-methyl-1,4-benzoquinone, Q0M 2,3-dimethoxy-5,6-dimethyl-1,4-benzoquinone, and Q1 2,3-dimethoxy-5-methyl-6-isoprenyl-1,4-benzoquinone.

In this scheme, k_{AP} and k_{BP} are the rates of the direct recombination routes for Q_A and Q_B, respectively, and K_{AB} is the equilibrium constant between the two radicals. For RCs in which UbiQ is acting as Q_A and Q_B, $k_{AP} \gg k_{BP}$. Thus, the rate of charge recombination when both Q_A and Q_B are bound (k_P) can be approximated as $k_P \approx k_{AP}/(1 + K_{AB})$.[59] Because k_P is typically an order of magnitude slower than in the case where Q_B is not present (k_{AP}), the back reaction kinetics can provide a convenient assay of how much Q_B was bound at the time of the actinic flash.

In this experiment, the ability of 3MeO-Q to compete with UbiQ-4 for the Q_B site is determined with a competitive binding assay. UbiQ-4 was chosen for this experiment because it has the same isoprenoid tail length as 3MeO-Q. RCs with UbiQ-4 acting as Q_B give a back reaction rate constant k_P upon light activation, whereas RCs with 3MeO-Q bound as Q_B will back react at a rate k_{AP} because Q_A^- to Q_B electron transfer does not occur for this quinone analogue. With UbiQ-4 analogues, quinone exchange between micelles occurs on the time scale of the back reaction. This makes the kinetics polyphasic, preventing a quantification of the amount of UbiQ-4 bound at Q_B from the relative amplitudes of the slow (k_P) and fast (k_{AP}) phases. In this case, the average lifetime is used instead as a good indicator of Q_B binding, where a faster back reaction indicates that more UbiQ-4 is being displaced by 3MeO-Q from the Q_B site.

Q_B-extracted RCs were prepared, leaving the Q_A site intact with the native, tightly bound UbiQ-10. The Q_B site was then filled with UbiQ-4 by titration from an ethanol stock. 3MeO-Q was then titrated from an ethanol stock into the cuvette while the average lifetime of the 430 nm back reaction kinetics of the charge recombination was being monitored. The final ethanol concentration at the end of the titration was 6%. The concentration of 3MeO-Q was increased from 0 to 600 μM, with a fixed concentration of 1.6 μM Q_B-extracted RCs and 3 μM UbiQ-4 in a pH 7.8 solution of 0.045% LDAO and 10 mM Tris.

RESULTS AND DISCUSSION

Three main categories of results will be presented: (1) the validation of the quinone parameter set against previously measured experimental observables, (2) the calculation of relative binding affinities between UbiQ and MMQ derivatives in the Q_A and Q_B sites, including comparisons with experimental observables, and (3) the observed behavior of quinones within the Q_A and Q_B sites during the equilibrium simulations.

Parameter Validation of Ubiquinone and Derivatives. One basic parameter validation step is to calculate the solvation free energy of the parameterized compounds. While experimental solvation free energies are available for a wide variety of model compounds,[60] quinones are not among them. Instead, we use the computed solvation free energies of quinones with varying tail lengths (Table 1) to compute the partition coefficient, log P, which provides a measure of solute partitioning between organic and aqueous phases. Comparison between our calculated log P values and previously reported experimental measurements[44] yields excellent agreement for octanol/water partitioning, coinciding with experimental values within the statistical error of our simulations. By contrast, the partition coefficients for cyclohexane/water partitioning are 1−1.5 log P units skewed in favor of partitioning into water for the most hydrophilic quinone, which may be due to the nonpolarizable nature of the force field not accounting for the induced dipoles and quadrupoles in hexane or cyclohexane caused by the quinone. The magnitude of the error is similar to that found in computational measures of other species that would induce dipoles, such as chlorinated benzene rings in a fixed-charge force field.[61,62] These cases are also found to partition too favorably into water.[61,62] The permanent dipole of octanol better represents the membrane interface, suggesting that the essential interactions of the quinones have been captured.

Prior studies have highlighted the difficulty in reproducing the methoxy dihedral angles of neutral UbiQ within the regime of a fixed-charge force field.[34] In addition to the solvation free energy, we have also compared our observed methoxy dihedral angles from equilibrium protein-bound simulations to distributions observed from the highest-resolution structures of UbiQ in the RC of *R. sphaeroides* (Figure 4). The degree to which our methoxy dihedral distributions overlap with the corresponding distributions from the PDB varies depending on the specific dihedral. The general trend is for the dihedral distributions from 2MeO-Q and 3MeO-Q simulations to show maxima that are in reasonable agreement with the maxima observed in the PDB distribution, while the distribution for UbiQ shows a less robust overlap. Within the crowded protein environment, the methoxy group orientation is determined by interactions with the protein, in addition to steric interactions between the two methoxy groups in UbiQ. The balance of these effects is delicate, and small errors can shift the distribution relative to experimentally observed PDB distributions. For UbiQ, the methyl moieties of the methoxy groups are frequently located on opposite sides of the quinone plane to minimize steric clashes (resulting in dihedral angles that are both either >0° or <0°), including states in which the methoxy is nearly coplanar because of the position of the methoxy torsion minima at planar geometries (see Methods). These states are not represented in a majority of crystallographic structures.

Because of steric interactions between the methoxy groups, the observed peak positions in the UbiQ dihedral distributions are in the correct locations; however, the size of these peaks

DOI: 10.1021/acs.biochem.5b00033
Biochemistry 2015, 54, 2104−2116

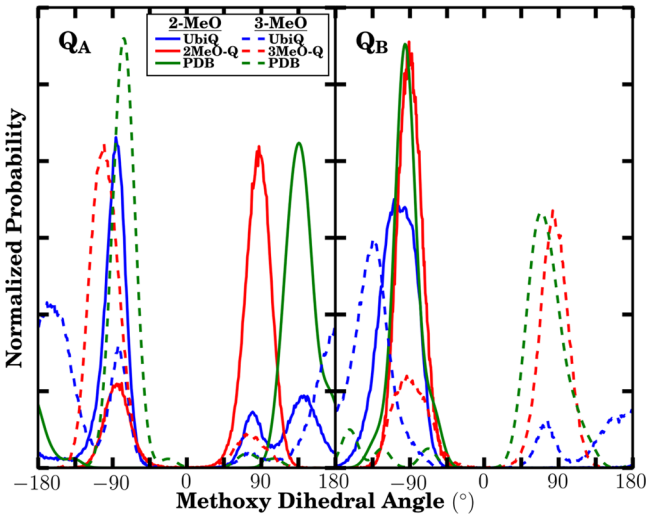

Figure 4. Methoxy dihedral angle distributions from the quinones occupying the Q_A (left) and Q_B (right) sites in our simulations (blue and red lines for UbiQ and MMQ distributions, respectively) are compared to the same dihedral angles present in the PDB (green). Solid lines indicate the distributions of the 2-methoxy group, while dashed lines are the distributions for the 3-methoxy group. For both methoxy groups, the dihedral is measured with respect to the adjacent carbonyl carbon, that is, C1 for the 2-methoxy group and C4 for the 3-methoxy group (Figure 2). The comparison green lines were determined by using 69 Q_A and 32 Q_B structures of available PDB structures (with a resolution better than 2.8 Å) where the quinone was in the proximal position (as indicated by a hydrogen bond distance of <4 Å to its histidine hydrogen bonding partner). To build the distribution, each PDB value was assumed to be a Gaussian with a σ of 10°.

relative to the predominant peak suggests a population shift of approximately 1 kcal/mol in favor of the crystallographically rare states. This population shift is consistent in magnitude with studies comparing the amino acid side chain rotameric states between MD simulation and their distributions within the PDB.[63] However, for the 2-methoxy dihedral angle in Q_B, we see close agreement between the simulation results and the distribution from the PDB, likely because of a hydrogen bond with the surrounding protein environment that will be discussed later in depth. Finally, we note that it is not surprising to detect a wider distribution or even new states and populations when one examines the system at ambient temperatures, as is the case in our simulation, in comparison to crystallographic structures representing a population at very low temperatures.

Differential Quinone Binding Affinity in RC Q_A and Q_B Sites. RCs occupied by 3MeO-Q are unable to undergo inter-quinone electron transfer.[12] Two potential hypotheses that might rationalize this observation exist. One posits that 3MeO-Q, which lacks a 2-methoxy group, simply does not bind to the Q_B site, thereby preventing inter-quinone electron transfer. However, prior experiments cannot exclude the possibility that 3MeO-Q does bind to Q_B and that the redox potential relative to Q_A is simply unfavorable when 3MeO-Q is bound. Our simulation results for the relative binding affinities (Table 2) show a ∼1.1 kcal/mol loss of binding free energy when going from UbiQ to 3MeO-Q in the Q_B site, which is in sharp contrast to the other relative binding free energies that show negligible differences. Upon comparison to a solution-based reference state, the other three UbiQ → MMQ combinations suggest tighter binding for the MMQ than for UbiQ. Because 2MeO-Q and 3MeO-Q lack one oxygen relative to UbiQ, they are more hydrophobic, and therefore, MMQ species are generally expected to bind the RC tighter than UbiQ when using an aqueous solution as the reference. However, as will be discussed in greater detail later, 3MeO-Q in the Q_B site lacks a strong favorable interaction that UbiQ has between the 2-methoxy oxygen and a specific residue on the protein backbone. As a result, 3MeO-Q binds less tightly in Q_B than UbiQ, despite its increased hydrophobicity.

The aqueous solubility of native quinones is quite poor because of their long isoprenoid tails, so quinones are known to partition strongly to the membrane.[44] To take this aspect into account, we also calculated the relative binding free energy when considering quinones at the membrane interface as the reference state ($\Delta\Delta G^{m\to p}_{UbiQ\to MMQ}$ in Table 2). The MMQs partition into the membrane more favorably than UbiQ by approximately 0.5 kcal/mol ($\Delta\Delta G^{s\to m}_{UbiQ\to MMQ}$ values of −0.60 ± 0.03 for 2MeO-Q and −0.46 ± 0.05 for 3MeO-Q) because of the absence of a single oxygen in MMQ relative to UbiQ. Because the quinone pool is predominantly membrane-bound *in vivo*, $\Delta\Delta G^{m\to p}_{UbiQ\to MMQ}$ may represent a better estimate of the relative binding affinities than $\Delta\Delta G^{s\to p}_{UbiQ\to MMQ}$.

In the three cases of well-bound MMQs, the mean $\Delta\Delta G^{m\to p}_{UbiQ\to MMQ}$ is very close to $-{}^1/_2RT$, which is the expected entropic stabilization from populating one internal degree of freedom. UbiQ has an additional dihedral torsion to consider relative to MMQs, and within the confines of the protein, the sampling of the methoxy dihedral angle is retarded, similar to the slowdown observed for protein rotameric transitions when the side chain is buried.[63] As detailed in the Supporting Information, we do not believe we have adequately sampled this additional slowly varying dihedral within the confines of the

Table 2. Relative Binding Affinities (in kilocalories per mole) Determined by Thermodynamic Integration for the Transformation of Ubiquinone (UbiQ) into a Monomethoxy Quinone (MMQ) between the Solution (s) or the Membrane (m) and the RC (p) ($\Delta\Delta G^{s\to p}_{UbiQ\to MMQ}$ and $\Delta\Delta G^{m\to p}_{UbiQ\to MMQ}$, respectively)[a]

site	MMQ	$\Delta\Delta G^{s\to p}_{UbiQ\to MMQ}$	$\Delta\Delta G^{m\to p}_{UbiQ\to MMQ}$	$\Delta\Delta G^{m\to p}_{UbiQ\to MMQ} + {}^1/_2RT$	k_d^{MMQ}/k_d^{UbiQ}
Q_A	2MeO-Q	−0.94 ± 0.01	−0.35 ± 0.03	−0.04 ± 0.03	0.9
	3MeO-Q	−0.70 ± 0.01	−0.23 ± 0.05	0.08 ± 0.05	1.1
Q_B	2MeO-Q	−0.88 ± 0.01	−0.28 ± 0.03	0.02 ± 0.05	1.0
	3MeO-Q	0.39 ± 0.02	0.85 ± 0.05	1.16 ± 0.05	6.6

[a]The ratio between the dissociation constants is related to $\Delta\Delta G$ by $k_d^{MMQ}/k_d^{UbiQ} = \exp[(\Delta\Delta G^{m\to p}_{UbiQ\to MMQ} + {}^1/_2RT)/RT]$, with the factor of ${}^1/_2RT$ emerging to correct for a systematic bias due to limited sampling (see the Supporting Information). Relative binding free energies ($\Delta\Delta G$) are calculated as follows: $\Delta G^{m\to p}_{MMQ} - \Delta G^{m\to p}_{UbiQ} = \Delta G^{p}_{UbiQ\to MMQ} - \Delta G^{m}_{UbiQ\to MMQ} = \Delta\Delta G^{m\to p}_{UbiQ\to MMQ}$, and $\Delta G^{s\to p}_{MMQ} - \Delta G^{s\to p}_{UbiQ} = \Delta G^{p}_{UbiQ\to MMQ} - \Delta G^{s}_{UbiQ\to MMQ} = \Delta\Delta G^{s\to p}_{UbiQ\to MMQ}$, using the states defined in Figure 3.

DOI: 10.1021/acs.biochem.5b00033
Biochemistry 2015, 54, 2104−2116

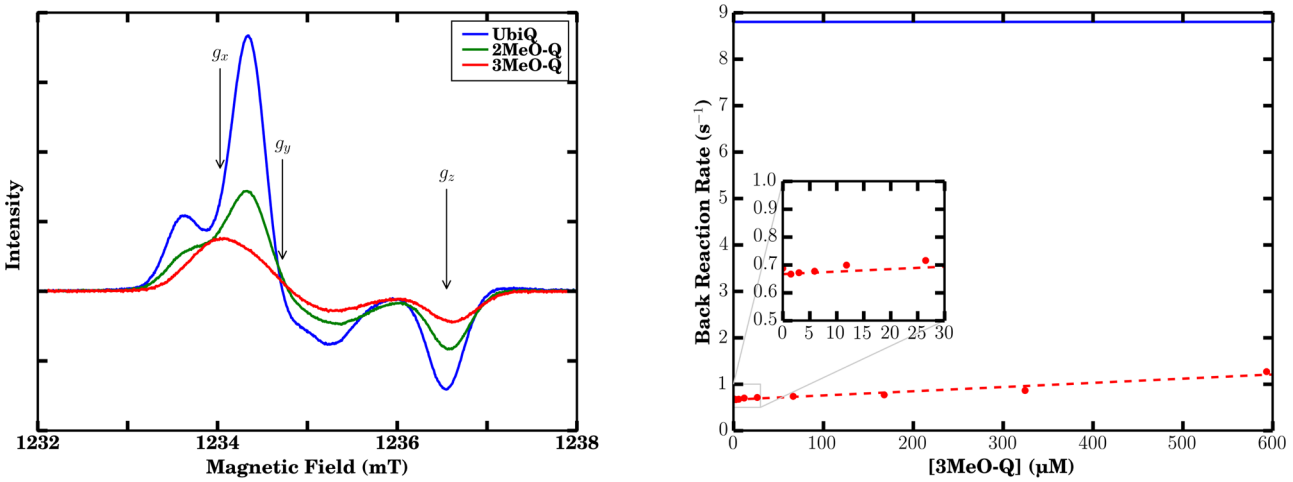

Figure 5. EPR and competitive binding assay. (Left) Continuous wave (CW) Q-band EPR spectra of quinone species formed in borohydride-reduced RCs reconstituted with MMQs at pH 10.5. Spectral components g_x, g_y, and g_z are expected to appear where indicated. Experimental settings: microwave frequency, 34.63 GHz; modulation amplitude, 0.2 mT; temperature, 90 K. (Right) Observed back reaction rate constant as a function of 3MeO-Q concentration in RCs, where 3MeO-Q competes with UbiQ-4 to act as Q_B. The data are essentially linear (red) across the concentration range considered. Shown in blue is the Q_A back reaction rate (8.8 s^{-1}) for these RCs when Q_B is unoccupied. Sample conditions: 1.6 μM RC, 3 μM UbiQ-4, 0.045% LDAO, 10 mM Tris, pH 7.8.

protein, so we account for this additional degree of freedom by adding $^1/_2RT$ to $\Delta G^p_{UbiQ\rightarrow MMQ}$ in Table 2.

It should be noted that even in the absence of this correction, the relative binding free energies follow the trend that holds that 3MeO-Q in the Q_B site binds less favorably than UbiQ, qualitatively consistent with the hypothesis that poor binding of 3MeO-Q to the Q_B site contributes to its inactivity in electron transfer. However, we use the corrected relative binding free energies to estimate the ratio of the dissociation constants between MMQs and UbiQ. The ratios in Table 2 indicate that the binding affinities between MMQs and UbiQ are similar, with the exception of 3MeO-Q in the Q_B site, where the calculated ratio of dissociation constants is 6.6, suggestive of mildly weaker binding by less than an order of magnitude.

Experimental Comparisons. From the TI calculation, we observe that 3MeO-Q exhibits binding to the Q_B site weaker than that of either 2MeO-Q or UbiQ, consistent with its behavior as an acceptable substitute in Q_A but not Q_B.[12] This can be compared to the CW EPR spectra of borohydride-reduced RCs with the native quinone (UbiQ-10) and reconstituted with MMQ (Figure 5), where the spectra strongly depend on the chemical identity of the quinone present. With UbiQ-10, the Q-band spectrum is in good agreement with previously reported spectra for the $Q_A^-Q_B^-$ biradical,[57] exhibiting additional splittings of the g_x and g_y spectral components resulting from the dipole−dipole and exchange interaction of two closely located electron spins. When the RC was reconstituted with 2MeO-Q, a splitting of the g_x and g_y components was still observed, indicating formation of the $Q_A^-Q_B^-$ biradical. The lower spectral resolution of the MMQ spectra in comparison with the resolution of the spectra of UbiQ-10 is likely due to the influence of the additional ring−methyl proton hyperfine coupling present in the MMQs, and the overall weaker signal suggests the $Q_B^{2-} \leftrightarrow Q_A^-Q_B^-$ equilibrium is shifted more toward quinol formation at pH 10.5.

In contrast, when the RC is reconstituted with 3MeO-Q, no splittings indicating formation of the $Q_A^-Q_B^-$ biradical are observed. Instead, independent pulsed EPR measurements assigned this signal to Q_A^- based on its similarity to previously determined Q_A^- spectra rather than Q_B^-[64,65] (Figure S3 of the Supporting Information). Borohydride is a two-electron donor and does not react with the one-electron donor−acceptor Q_A. Therefore, for RCs reconstituted with 3MeO-Q, Q_A^- could only have been formed by electron disproportionation from Q_B^{2-}. $Q_A^-Q_B^-$ is necessarily formed at least transiently during this process, and the lack of any observable Q_B^- signal indicates this semiquinone is highly unstable and dissociates quickly upon biradical formation. This is in contrast to UbiQ-10 and 2MeO-Q, where Q_B^- is stable enough to observe the biradical. Evidently, the 2-methoxy group plays a substantial role in the binding affinity of UbiQ in its semiquinone form for the Q_B binding pocket.

The weaker Q_B binding affinity of 3MeO-Q suggested by the CW Q-band EPR experiments can be quantitated with a competitive binding assay. By titrating in nonfunctional 3MeO-Q and observing the rate of charge recombination, we can estimate the relative binding affinities of 3MeO-Q and UbiQ. In our case, a back reaction rate of 8.8 s^{-1} was found for RCs with only Q_A activity, and upon addition of 3 μM UbiQ-4 to activate Q_B, the rate decreased to 0.7 s^{-1}. Addition of 3MeO-Q, which inhibits Q_B activity, is expected to increase the back reaction rate from 0.7 s^{-1} (up to a maximum of 8.8 s^{-1}) as it competes with the UbiQ-4 bound at the Q_B site. An increase in the back reaction rate constant is observed as a function of 3MeO-Q concentration (Figure 5). However, the inhibition of Q_B activity by 3MeO-Q is very weak, and essentially linear over the concentration range considered. The binding of 3MeO-Q for the Q_B site is estimated to be more than 1000 times weaker than that of UbiQ-4.

These experimental results are qualitatively consistent with the TI calculations but are inconsistent in terms of their magnitude, with computed binding affinity differences that are significantly smaller than what the experiment would suggest. Nevertheless, the overall conclusion and trends between the methods are the same; there is some protein−quinone interaction that makes 3MeO-Q binding unfavorable, which

DOI: 10.1021/acs.biochem.5b00033
Biochemistry 2015, 54, 2104−2116

Table 3. Hydrogen Bond Interactions between Quinones in the Q_A and Q_B Sites and the Surrounding Protein[a]

		hydrogen bond probability			average interaction distance (Å)		
Q site:atom	RC residue:atom	UbiQ	2MeO-Q	3MeO-Q	UbiQ	2MeO-Q	3MeO-Q
Q_A:O1	AlaM260:N	60.36	36.36	79.77	2.91 ± 0.00	3.15 ± 0.05	2.89 ± 0.01
Q_A:O4	HisM219:ND1	59.53	80.98	64.93	3.11 ± 0.02	2.92 ± 0.01	3.06 ± 0.01
Q_B:O1	IleL224:N	61.90	39.45	51.37	2.97 ± 0.01	3.06 ± 0.02	3.07 ± 0.03
Q_B:O2	GlyL225:N	17.66	4.73	–	3.31 ± 0.04	3.27 ± 0.01	3.72 ± 0.04
Q_B:O3	HisL190:ND1	0.34	–	3.93	4.28 ± 0.03	4.50 ± 0.02	4.25 ± 0.12
Q_B:O4	HisL190:ND1	38.37	75.08	23.19	3.07 ± 0.03	2.89 ± 0.01	3.23 ± 0.06

[a]Specific interactions are labeled according to the quinone atom using IUPAC nomenclature (Figure 2). The atom on the protein residue that participates in the hydrogen bond is also specified. The percentages of time during the simulations when the hydrogen bond was formed, defined to exist when the donor and acceptor heavy atoms are within 3.2 Å and the hydrogen is within 30° of the line between them, are reported. Note that 2MeO-Q and 3MeO-Q have blank entries in the Q_B site that correspond to the hydrogen bonds that are missing because of the absence of the appropriate hydrogen bond acceptor atom (O2 in the case of 3MeO-Q and O3 in the case of 2MeO-Q). In these cases, the interaction distance is calculated to the methyl carbon that replaces the methoxy oxygen. Animations of the quinones in the Q_A and Q_B sites are provided as Supporting Information.

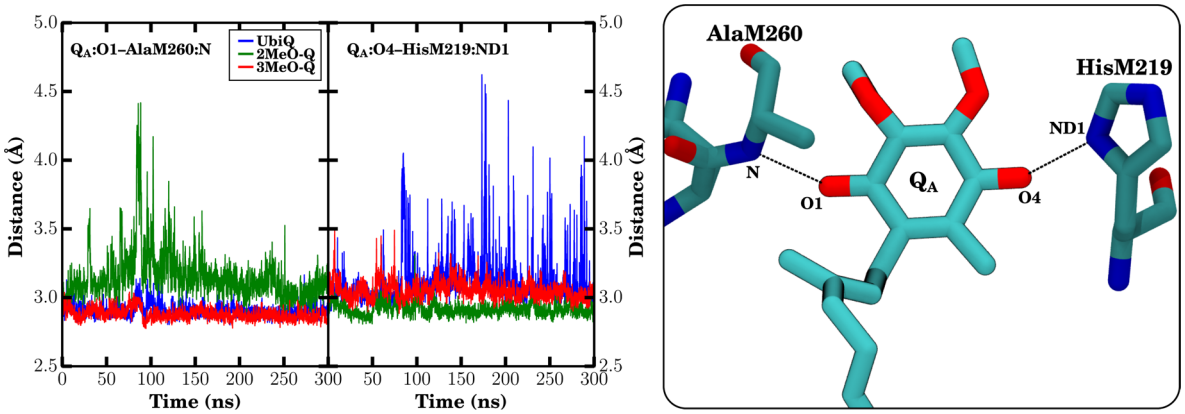

Figure 6. Interaction distances for carbonyl oxygen interactions in Q_A. The distance between the heavy atoms for each specific interaction was monitored over all three equilibrium trajectories (left). UbiQ is colored blue, 2MeO-Q green, and 3MeO-Q red. Individual data points are the running average over 100 ps of trajectory (the average of 50 frames with a 2 ps interval). On the right is a representative snapshot highlighting the exact distances that were measured. Because distances were measured only between heavy atoms, hydrogens are not shown.

we will detail below through our investigation of the equilibrium simulations.

Bound Quinone Conformations. To characterize structural dynamics of the quinones within their RC binding sites, we have analyzed the trajectories resulting from the equilibrium MD simulations of membrane-bound RCs. We observe modulation of specific interactions unique to each quinone species occupying the Q_A and Q_B sites. The primary stabilizing interactions between the RC and the quinones are known to be mediated by hydrogen bonds, and the observed interactions form a superset over the interactions determined through crystallographic[19,20,66] and EPR experiments.[64,67−69] We observe two predominant hydrogen bonds between the protein and the carbonyl oxygens of the quinones in their respective sites, as well as protein−methoxy interactions in Q_B (Table 3). The interactions are dependent on the unique electronic environment of the quinone around itself (Figure S4 of the Supporting Information). The specific hydrogen bonding interactions are detailed in the sections to follow.

Q_A Site. In Q_A, the only observed interactions are well-defined hydrogen bonds from AlaM260 and HisM219 to the two quinone carbonyl oxygens, with no strong hydrogen bonds between the methoxy groups and the RC. These interactions are described well by simple electrostatics[70] and have been extensively characterized in functional and crystallographic studies[67] and are also maintained in our simulations, as reflected by the short interatomic distances between hydrogen bonding partners in Q_A (Figure 6). The interaction distances observed in our simulations are very close to the interaction distances seen in prior QM/MM studies of neutral UbiQ.[70,71] The small differences can be attributed to thermal fluctuations of the system in our simulations, as opposed to the minimized geometries in the QM/MM calculations.[70,71] The distance between Q_A:O4 and HisM219:ND1 is 3.114 ± 0.001 Å, compared to 2.87 Å[70] and 2.81 Å.[71] The distance between Q_A:O1 and AlaM260:N is 2.908 ± 0.001 Å, compared to 2.84 Å[70] and 2.95 Å.[71] The overall sum of the distances between interaction partners in our simulations appears to be nearly conserved, with the longer interaction distance between Q_A:O1 and AlaM260 in 2MeO-Q compensated by the closer interaction of 2MeO-Q with HisM219, a relationship that suggests that the thermal stochastic motion of the quinone is along the vector connecting AlaM260 and HisM219.

The simulations suggest a dearth of specific interaction partners for the methoxy oxygens in Q_A. Other than steric interactions with the protein environment, no specific interactions were observed to modulate the methoxy dihedral angle. As a result, the exchange between the two orientations relative to the quinone plane is quite rapid and is observed frequently in our equilibrium simulations (Figure 7 and Table S2 of the Supporting Information).

DOI: 10.1021/acs.biochem.5b00033
Biochemistry 2015, 54, 2104−2116

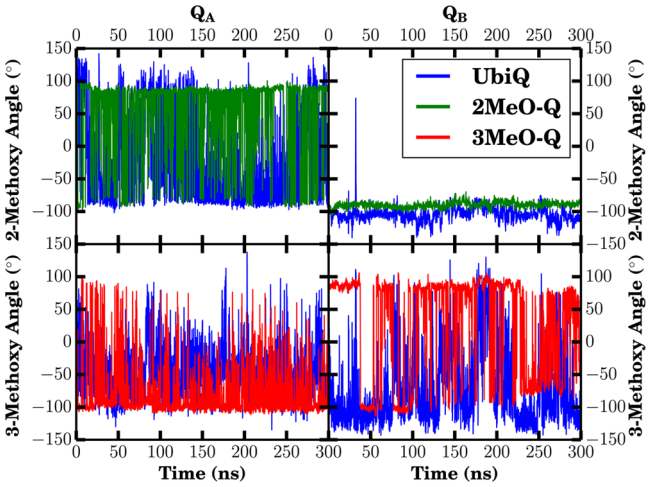

Figure 7. Methoxy dihedral angle over time for both Q_A (left) and Q_B (right). The dihedral angle for both 2-methoxy (top) and 3-methoxy (bottom) groups is measured with respect to the adjacent carbonyl carbon, C1 for the 2-methoxy group and C4 for the 3-methoxy group. Individual data points are the running average over 100 ps of trajectory (the mean of 50 frames with a 2 ps interval). The corresponding distributions of these dihedral angles are also shown in Figure 4.

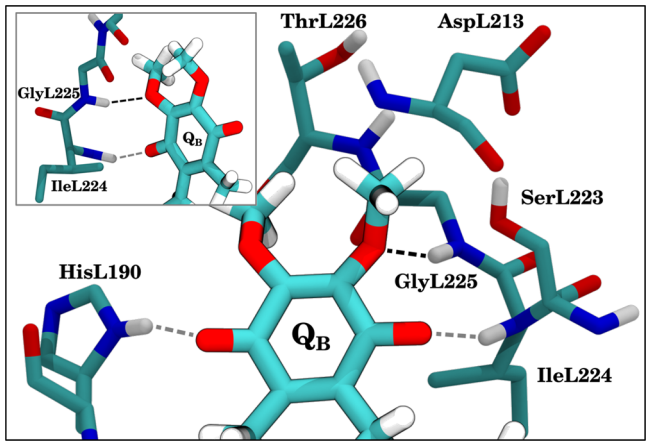

Figure 8. Quinone occupying the Q_B site, along with its interaction partners and other relevant residues. Carbons are colored cyan, oxygens red, nitrogens blue, and hydrogens white. UbiQ is drawn with a black outline and more brightly than the surrounding protein residues. The three predominant hydrogen bonds are indicated by dashed lines. The interaction of the 2-methoxy oxygen with GlyL225 is colored black, while the other hydrogen bonds are colored gray. The hydrogen bonds to GlyL225 and IleL224 are highlighted in the inset, which shows a rotated view of the main figure with only L224–L226 provided for context.

Q_B Site. The quinone occupying the Q_B site has a functional role different from that of Q_A, as it is the quinone that is reduced to quinol and exchanges with the quinone pool in the membrane. However, the primary quinone–protein interactions observed in the Q_B site are quinone carbonyl and protein interactions analogous to the interactions in the Q_A site. The hydrogen bond between quinone carbonyl oxygen Q_B:O4 and HisL190 is well-established.[66] The identity of the hydrogen bonding partner(s) opposite HisL190 in Q_B is a matter of debate. From available crystal structures, the residues that might form interactions with carbonyl oxygen Q_B:O1 are ambiguous.[20,66] Some structures also show the quinone in a nonfunctional site distal to the iron but still within the RC, rather than in the site proximal to the iron that is thought to be the active state. For structures in which the quinone is proximal to the iron, SerL223, IleL224, and GlyL225 have each been suggested as potential candidates for the interaction partner with Q_B:O1. We do not detect any significant interaction between SerL223 and the quinone within our simulations. SerL223 has been suggested by mutagenesis and EPR experiments[72−74] to be involved in proton transfer from solution to the quinone. When AspL213 is deprotonated in our simulations, SerL223 interacts with AspL213, a state that has previously been shown computationally to be favored for deprotonated AspL213.[73,75,76] The most significant O1 interactions are formed with IleL224 across all three simulated quinones (Table 3 and Figures 8 and 9).

In addition to the carbonyl interactions, our simulations suggest an interaction unique to the Q_B site between the 2-methoxy oxygen and the protein environment. Specifically, there is a detectable and prevalent hydrogen bond between Q_B:O2 and the backbone amino group of GlyL225 (Table 3), with the methoxy oxygen as the acceptor of the amide hydrogen (Figure 8). Deviations in the interaction distance are small around its equilibrium length of ∼3.3 Å in the UbiQ and 2MeO-Q simulations where the 2-methoxy oxygen is present (Figure 9 and Table 3). Because of the electrostatic interaction with GlyL225, the 2-methoxy group is effectively locked in place, as it cannot flip without disrupting the favorable hydrogen bond and placing the methoxy methyl into the space occupied by GlyL225. As a result, only a single instance of 2-methoxy flipping in the Q_B site was observed (Figure 7 and Table S2 of the Supporting Information). The hydrogen bond between GlyL225 and the methoxy oxygen in Q_B may be the structural mechanism whereby the 2-methoxy dihedral angle is kept further out of plane, thereby breaking the symmetry between the Q_A and Q_B quinones, and is essential[9] for generating the observed 60–80 mV redox potential difference.[3,4] When the methoxy group is out of plane, it withdraws electrons from the ring, increasing the redox potential relative to that of an in-plane conformation where the methoxy oxygen p-orbitals conjugate with those in the ring, donating electrons instead, particularly to C3 of the ring (Figure S2B of the Supporting Information). Previous studies have shown that this effect contributes in excess of 160 mV to the redox potential difference between Q_A and Q_B.[9] Thus, this hydrogen bond may be essential to generating a redox potential difference for efficient electron transfer between the two quinones.

In 3MeO-Q, where the 2-methoxy group is replaced with a methyl, the hydrogen bonding interaction with GlyL225 is abolished. The observed distances between the Q_B:O1 carbonyl oxygen and IleL224 are comparable across all three quinones; the distance between GlyL225 and the 2-methyl carbon in 3MeO-Q is increased, as otherwise the hydrogens from the methyl and the backbone of this residue would clash (Figure 9 and Table 3). The 3-methoxy oxygen of 3MeO-Q forms sporadic interactions with HisL190, as indicated by interaction distances of <3.5 Å in Figure 9, and this competing interaction lengthens the average distance between carbonyl oxygen O4 and HisL190 (Table 3).

The observed small changes in the interaction pattern caused by replacement of a methoxy group with a methyl group cause minor perturbations to the position of the quinone in the Q_B site. The root-mean-square deviation (rmsd) relative to the available crystallographic structures for quinones within the Q_B

DOI: 10.1021/acs.biochem.5b00033
Biochemistry 2015, 54, 2104–2116

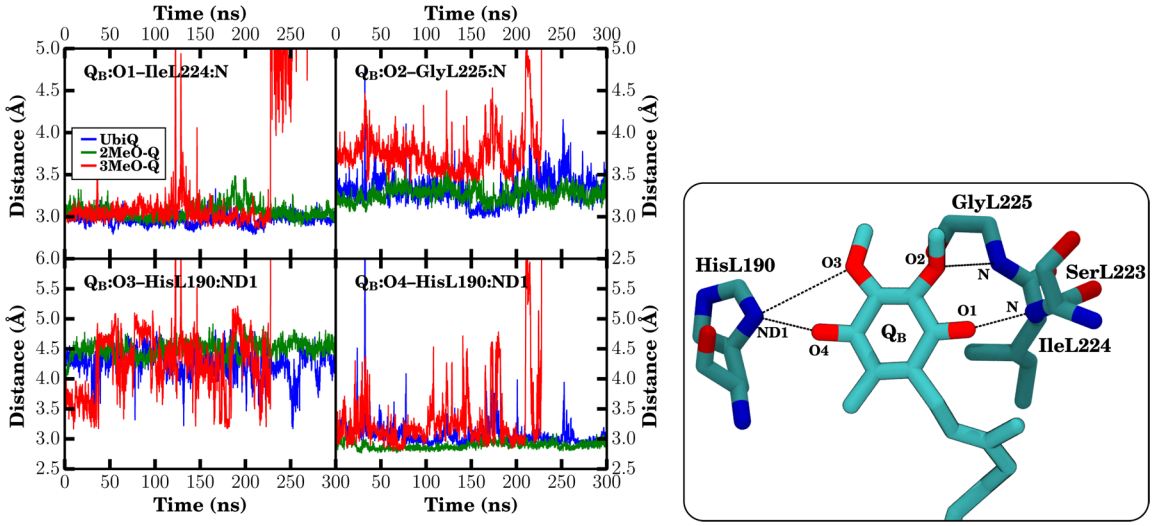

Figure 9. Interaction distances for oxygen interactions in Q_B. In the right panel, the distance between the heavy atoms for each specific interaction was monitored over all three equilibrium trajectories. If the oxygen is missing for a particular interaction, i.e., when a methyl group replaces a methoxy group in MMQs, the distance was determined on the basis of the methyl carbon that replaced it. Distances for UbiQ, 2MeO-Q, and 3MeO-Q are colored blue, green, and red, respectivelyin the time series. The left panels show snapshots highlighting the specific distances measured. Because distances were measured only between heavy atoms, hydrogens are not shown. Note that 3MeO-Q moves to the distal site after 225 ns, shifting the interaction distances up by 4−6 Å (see also Figure S6 of the Supporting Information). Individual data points are the running average over 100 ps of trajectory (the average of 50 frames with a 2 ps interval).

site is rather small (Table 4 and Figure S7 of the Supporting Information), with a mean rmsd of <1 Å between the ring carbons of the quinone headgroups seen in simulation and conformations identified crystallographically. Despite being small, the rmsd in the case of 3MeO-Q is substantially larger than the rmsds for UbiQ or 2MeO-Q, exhibiting larger average displacements and deviations from the crystallographic proximal (active, quinone near the iron) states (Table 4). We hypothesize that the origin of the increased displacement is due to steric interactions between GlyL225 and the methyl group replacing the 2-methoxy group in 3MeO-Q changing the equilibrium position slightly, as supported by the altered interaction distances in Q_B (Table 3). The binding site perturbations for 3MeO-Q in the Q_B site support the free energy calculations that suggest a lower binding affinity for 3MeO-Q relative to those of the other simulated quinones (Table 2). The larger variability in quinone position for 3MeO-Q suggests that the transition barrier between the sites proximal and distal to the iron (Figure 1) in Q_B may be easily surmountable at physiological temperatures, which is strongly supported by the observed movement of 3MeO-Q to the distal site after 225 ns (Figure 9 and Figures S6 and S7 of the Supporting Information). The expectation is that 3MeO-Q would have a substantially shorter mean lifetime (less than ∼1 μs) within the proximal position of the Q_B site relative to that of either 2MeO-Q or UbiQ (>1 ms).[77]

Table 4. Root-Mean-Square Deviations (rmsd) and Displacements (d) for the Quinone Ring Carbons Occupying the Q_B Site Calculated from the Simulations Relative to the Proximal Q_B Position Observed in the 32 *R. sphaeroides* RC Crystal Structures with Better Than 2.8 Å Resolution[a]

quinone	rmsd (Å)	d (Å)
UbiQ	0.75 ± 0.27	0.65 ± 0.29
2MeO-Q	0.72 ± 0.18	0.57 ± 0.19
3MeO-Q	0.97 ± 0.38	0.89 ± 0.40

[a]The reported mean (μ) and standard deviations (σ) exclude the case in which 3MeO-Q was in the distal site; however, for UbiQ and 2MeO-Q, the entire 300 ns trajectory was considered when computing the average.

Interaction Partners for SerL223 after Protonation of AspL213. In the simulations described to this point, AspL213 was deprotonated and was the predominant hydrogen bonding partner for the hydroxyl group of SerL223. SerL223 has been established to play a role in proton transfer, providing a hydrogen to reduce the semiquinone radical to form the appropriate quinol. The orientation of SerL223 has been shown to depend on several factors. Some crystallographic structures suggest that SerL223 interacts via a hydrogen bond with the quinone,[19,20,66] whereas electrostatics calculations suggest that deprotonated AspL213 might be the significant partner to SerL223,[73,75,76] consistent with what we observe in our deprotonated simulations. In our additional simulation of UbiQ in the Q_A and Q_B sites with protonated AspL213, SerL223 shifts from interacting with AspL213 to ArgL217 (Table S5 of the Supporting Information). Interactions between SerL223 and UbiQ still form, but only for a small fraction of time (<0.2%), contrary to what might be inferred from the shorter bond between SerL223 and UbiQ seen crystallographically (Table S3 of the Supporting Information). Given the role of GlyL225 in interacting with the 2-methoxy group and no observed SerL223−UbiQ interactions, our interpretation is that the predominant Q_B quinone carbonyl interaction across from HisL190 is IleL224 in the neutral state. This differs from the semiquinone state, in which GlyL225 has been suggested to be the primary carbonyl interaction parter,[64] and may indicate a small quinone rearrangement upon semiquinone formation.

DOI: 10.1021/acs.biochem.5b00033
Biochemistry 2015, 54, 2104−2116

CONCLUSIONS

After reparameterization of the quinone force field, we have investigated the specific interactions between the protein environment and UbiQ that might be responsible for breaking the symmetry and generating the redox potential difference in the two quinone binding sites within the RC of *R. sphaeroides*. The simulations performed are the longest simulations to date of a membrane-bound bacterial RC by 2 orders of magnitude, with 300 ns of simulation for each of the three quinone analogues studied. These simulations indicate that the 2-methoxy oxygen of the Q_B quinone forms an interaction with the backbone amide of GlyL225, while the carbonyl oxygen opposite of HisL190 hydrogen bonds with the backbone of IleL224. This interaction pattern serves to break the symmetry of neutral UbiQ between Q_A and Q_B by locking the 2-methoxy dihedral angle of Q_B in a position conducive to electron transfer from Q_A to Q_B. 3MeO-Q lacks this 2-methoxy oxygen and therefore exhibits weaker binding to the Q_B site than either UbiQ or 2MeO-Q, consistent with its observed nonfunctionality as an electron acceptor in Q_B,[12] the weak binding shown through TI calculations and spontaneous unbinding in equilibrium, its poor competition for the Q_B site, and a lack of any observable $Q_A^-Q_B^-$ biradical signal in the CW EPR spectrum upon borohydride reduction at pH 10.5. In addition, we determined that SerL223 does not form direct interactions with the neutral quinone either with or without the protonation of AspL213, suggesting that its role as the proton donor in the formation of quinol is mediated by the formation of the semiquinone or biradical, as has been postulated previously.[75] These mechanistic details may not be unique to the RC and are a clear example of the detailed interactions that lie at the heart of protein redox chemistry.

ASSOCIATED CONTENT

Supporting Information

Final topology and parameter files for quinones, additional discussion regarding the need for orientational restraints during TI calculations and the origins of the $^1/_2RT$ correction in Table 2, large or ancilliary tables and figures, and animations detailing the interactions in the Q_A and Q_B sites are provided. This material is available free of charge via the Internet at http://pubs.acs.org.

AUTHOR INFORMATION

Corresponding Author

*E-mail: emad@life.illinois.edu.

Present Address

[@]A.T.T.: Department of Biochemistry and Molecular Biology, Nippon Medical School, Sendagi, Bunkyo-ku, Tokyo 113-8602, Japan.

Funding

The computational work was supported by the grants from the National Institutes of Health (NIH) to E.T. (U54-GM087519 and P41-RR05969), grants from the National Science Foundation to C.A.W. (MCB-0818121), and a U.S. Department of Energy CSGF Fellowship to J.V.V. (DE-FG02-97ER25308). S.A.D. acknowledges Grant DE-FG02-08ER15960 from the U.S. Department of Energy, Office of Science, Office of Basic Energy Sciences, Chemical Sciences, Geosciences and Biosciences Division, to support the EPR studies. J.V.V. and A.T.T. acknowledge past support from NIH Molecular Biophysics Training Grants.

Notes

The authors declare no competing financial interest.

[⊥]C.A.W.: Deceased July 10, 2014.

ACKNOWLEDGMENTS

This research used resources of the National Energy Research Scientific Computing Center (NERSC), which is supported by the Office of Science of the U.S. Department of Energy under Contract No. DE-AC02-05CH11231. This research also was conducted through the use of the parallel computing resource Taub provided by the Computational Science and Engineering Program at the University of Illinois. Additional simulations were performed using Stampede, hosted at the Texas Advanced Computing Center (TACC) at The University of Texas at Austin through XSEDE (grant number MCA06N060 to E.T.) funded by NSF.

REFERENCES

(1) Wraight, C. A., and Gunner, M. R. (2009) in *The Purple Phototrophic Bacteria* (Hunter, C. N., Daldal, F., Thurnauer, M. C., and Beatty, J. T., Eds.) Advances in Photosynthesis and Respiration, Vol. *28* pp 379−405, Springer, Dordrecht, The Netherlands.

(2) Okamura, M., Paddock, M., Graige, M., and Feher, G. (2000) Proton and electron transfer in bacterial reaction centers. *Biochim. Biophys. Acta 1458*, 148−163.

(3) Wraight, C. A. (1979) Electron acceptors of bacterial photosynthetic reaction centers. II. H^+ binding coupled to secondary electron transfer in the quinone acceptor complex. *Biochim. Biophys. Acta 548*, 309−327.

(4) Kleinfeld, D., Okamura, M. Y., and Feher, G. (1984) Electron transfer in reaction centers of *Rhodopseudomonas sphaeroides*. I. Determination of the charge recombination pathway of $D_+Q_AQ_B^-$ and free energy and kinetic relations between $Q_A^-Q_B$ and $Q_AQ_B^-$. *Biochim. Biophys. Acta 766*, 126−140.

(5) Prince, R. C., Dutton, P., and Bruce, J. (1983) Electrochemistry of ubiquinones. *FEBS Lett. 160*, 273−276.

(6) Allen, J. P., Feher, G., Yeates, T. O., Komiya, H., and Rees, D. C. (1987) Structure of the reaction center from *Rhodobacter sphaeroides* R-26: The cofactors. *Proc. Natl. Acad. Sci. U.S.A. 84*, 5730−5734.

(7) Ke, B. (2001) *Photosynthesis: Photobiochemistry and Photobiophysics*, Kluwer Academic Publishers, Boston.

(8) Taguchi, A. T., O'Malley, P. J., Wraight, C. A., and Dikanov, S. A. (2013) Conformational differences between the methoxy groups of Q_A and Q_B site ubisemiquinones in bacterial reaction centers: A key role for methoxy group orientation in modulating ubiquinone redox potential. *Biochemistry 52*, 4648−4655.

(9) Taguchi, A. T., Mattis, A. J., O'Malley, P. J., Dikanov, S. A., and Wraight, C. A. (2013) Tuning Cofactor Redox Potentials: The 2-Methoxy Dihedral Angle Generates a Redox Potential Difference of >160 mV between the Primary (Q_A) and Secondary (Q_B) Quinones of the Bacterial Photosynthetic Reaction Center. *Biochemistry 52*, 7164−7166.

(10) de Almeida, W. B., Taguchi, A. T., Dikanov, S. A., Wraight, C. A., and O'Malley, P. J. (2014) The 2-Methoxy Group Orientation Regulates the Redox Potential Difference between the Primary (Q_A) and Secondary (Q_B) Quinones of Type II Bacterial Photosynthetic Reaction Centers. *J. Phys. Chem. Lett. 5*, 2506−2509.

(11) Zhang, X., and Gunner, M. R. (2014) Affinity and activity of non-native quinones at the Q_B site of bacterial photosynthetic reaction centers. *Photosynth. Res. 120*, 181−196.

(12) Wraight, C. A., Vakkasoglu, A. S., Poluektov, Y., Mattis, A. J., Nihan, D., and Lipshutz, B. H. (2008) The 2-methoxy group of ubiquinone is essential for function of the acceptor quinones in reaction centers from *Rba. sphaeroides*. *Biochim. Biophys. Acta 1777*, 631−636.

DOI: 10.1021/acs.biochem.5b00033
Biochemistry 2015, 54, 2104−2116

(13) Ceccarelli, M., Procacci, P., and Marchi, M. (2003) An ab initio force field for the cofactors of bacterial photosynthesis. *J. Comput. Chem. 24*, 129−142.
(14) Damjanović, A., Kosztin, I., Kleinekathoefer, U., and Schulten, K. (2002) Excitons in a Photosynthetic Light-Harvesting System: A Combined Molecular Dynamics, Quantum Chemistry and Polaron Model Study. *Phys. Rev. E 65*, 031919.
(15) Nonella, M., and Schulten, K. (1991) Molecular Dynamics Simulation of Electron Transfer in Proteins: Theory and Application to $Q_A \rightarrow Q_B$ Transfer in the Photosynthetic Reaction Center. *J. Phys. Chem. 95*, 2059−2067.
(16) Cino, E. A., Choy, W.-Y., and Karttunen, M. (2012) Comparison of Secondary Structure Formation Using 10 Different Force Fields in Microsecond Molecular Dynamics Simulations. *J. Chem. Theory. Comput. 8*, 2725−2740.
(17) Vanommeslaeghe, K., Hatcher, E., Acharya, C., Kundu, S., Zhong, S., Shim, J., Darian, E., Guvench, O., Lopes, P., Vorobyov, I., and MacKerell, A. D., Jr. (2010) CHARMM General Force Field: A force field for drug-like molecules compatible with the CHARMM all-atom additive biological force fields. *J. Comput. Chem. 31*, 671−690.
(18) Mayne, C. G., Saam, J., Schulten, K., Tajkhorshid, E., and Gumbart, J. C. (2013) Rapid parameterization of small molecules using the Force Field Toolkit. *J. Comput. Chem. 34*, 2757−2770.
(19) Axelrod, H. L., Abresch, E. C., Paddock, M. L., Okamura, M. Y., and Feher, G. (2000) Determination of the binding sites of the proton transfer inhibitors Cd^{2+} and Zn^{2+} in bacterial reaction centers. *Proc. Natl. Acad. Sci. U.S.A. 97*, 1542−1547.
(20) Koepke, J., Krammer, E.-M., Klingen, A. R., Sebban, P., Ullmann, G. M., and Fritzsch, G. (2007) pH modulates the quinone position in the photosynthetic reaction center from *Rhodobacter sphaeroides* in the neutral and charge separated states. *J. Mol. Biol. 371*, 396−409.
(21) Phillips, J. C., Braun, R., Wang, W., Gumbart, J., Tajkhorshid, E., Villa, E., Chipot, C., Skeel, R. D., Kale, L., and Schulten, K. (2005) Scalable Molecular Dynamics with NAMD. *J. Comput. Chem. 26*, 1781−1802.
(22) Best, R. B., Zhu, X., Shim, J., Lopes, P. E. M., Mittal, J., Feig, M., and MacKerell, A. D. (2012) Optimization of the Additive CHARMM All-Atom Protein Force Field Targeting Improved Sampling of the Backbone ϕ, ψ and Side-Chain χ_1 and χ_2 Dihedral Angles. *J. Chem. Theory Comput. 8*, 3257−3273.
(23) Mackerell, A. D. (2004) Empirical force fields for biological macromolecules: Overview and issues. *J. Comput. Chem. 25*, 1584−1604.
(24) MacKerell, A. D., Jr., et al. (1998) All-atom empirical potential for molecular modeling and dynamics studies of proteins. *J. Phys. Chem. B 102*, 3586−3616.
(25) Klauda, J. B., Venable, R. M., Freites, J. A., O'Connor, J. W., Tobias, D. J., Mondragon-Ramirez, C., Vorobyov, I., MacKerell, A. D., Jr., and Pastor, R. W. (2010) Update of the CHARMM all-atom additive force field for lipids: Validation on six lipid types. *J. Phys. Chem. B 114*, 7830−7843.
(26) Jorgensen, W. L., Chandrasekhar, J., Madura, J. D., Impey, R. W., and Klein, M. L. (1983) Comparison of simple potential functions for simulating liquid water. *J. Chem. Phys. 79*, 926−935.
(27) Autenrieth, F., Tajkhorshid, E., Baudry, J., and Luthey-Schulten, Z. (2004) Classical force field parameters for the heme prosthetic group of cytochrome c. *J. Comput. Chem. 25*, 1613−1622.
(28) Darden, T., York, D., and Pedersen, L. G. (1993) Particle mesh Ewald: An $N\cdot\log(N)$ method for Ewald sums in large systems. *J. Chem. Phys. 98*, 10089−10092.
(29) Essmann, U., Perera, L., Berkowitz, M. L., Darden, T., Lee, H., and Pedersen, L. G. (1995) A smooth particle mesh Ewald method. *J. Chem. Phys. 103*, 8577−8593.
(30) Miyamoto, S., and Kollman, P. A. (1992) SETTLE: An Analytical Version of the SHAKE and RATTLE Algorithm for Rigid Water Molecules. *J. Comput. Chem. 13*, 952−962.
(31) Martyna, G. J., Tobias, D. J., and Klein, M. L. (1994) Constant Pressure Molecular Dynamics Algorithms. *J. Chem. Phys. 101*, 4177−4189.
(32) Feller, S. E., Zhang, Y., Pastor, R. W., and Brooks, B. R. (1995) Constant pressure molecular dynamics simulation: The Langevin piston method. *J. Chem. Phys. 103*, 4613−4621.
(33) Humphrey, W., Dalke, A., and Schulten, K. (1996) VMD: Visual Molecular Dynamics. *J. Mol. Graphics 14*, 33−38.
(34) Nilsson, J. A., Lyubartsev, A., Eriksson, L. A., and Laaksonen, A. (2001) Molecular dynamics simulations of ubiquinone; a survey over torsional potentials and hydrogen bonds. *Mol. Phys. 99*, 1795−1804.
(35) MacKerell, A. D., Brooks, B., Brooks, C. L., Nilsson, L., Roux, B., Won, Y., and Karplus, M. (2002) *Encyclopedia of Computational Chemistry*, John Wiley & Sons, Ltd., New York.
(36) Saer, R. G., Hardjasa, A., Rosell, F. I., Mauk, A. G., Murphy, M. E. P., and Beatty, J. T. (2013) Role of *Rhodobacter sphaeroides* photosynthetic reaction center residue M214 in the composition, absorbance properties, and conformations of H_A and B_A cofactors. *Biochemistry 52*, 2206−2217.
(37) Vasilieva, L. G., Fufina, T. Y., Gabdulkhakov, A. G., Leonova, M. M., Khatypov, R. A., and Shuvalov, V. A. (2012) The site-directed mutation I(L177)H in *Rhodobacter sphaeroides* reaction center affects coordination of P_A and B_B bacteriochlorophylls. *Biochim. Biophys. Acta 1817*, 1407−1417.
(38) Gibasiewicz, K., Pajzderska, M., Potter, J. A., Fyfe, P. K., Dobek, A., Brettel, K., and Jones, M. R. (2011) Mechanism of recombination of the $P^+H_A^-$ radical pair in mutant *Rhodobacter sphaeroides* reaction centers with modified free energy gaps between $P^+B_A^-$ and $P^+H_A^-$. *J. Phys. Chem. B 115*, 13037−13050.
(39) Frolov, D., Marsh, M., Crouch, L. I., Fyfe, P. K., Robert, B., van Grondelle, R., Hadfield, A., and Jones, M. R. (2010) Structural and spectroscopic consequences of hexacoordination of a bacteriochlorophyll cofactor in the *Rhodobacter sphaeroides* reaction center. *Biochemistry 49*, 1882−1892.
(40) Burie, J.-R., Boullais, C., Nonella, M., Mioskowski, C., Nabedryk, E., and Breton, J. (1997) Importance of the Conformation of Methoxy Groups on the Vibrational and Electrochemical Properties of Ubiquinones. *J. Phys. Chem. B 101*, 6607−6617.
(41) Asher, J. R., and Kaupp, M. (2008) Car-Parrinello molecular dynamics simulations and EPR property calculations on aqueous ubisemiquinone radical anion. *Theor. Chem. Acc. 119*, 477−487.
(42) Boullais, C., Nabedryk, E., Burie, J.-R., Nonella, M., Mioskowski, C., and Breton, J. (1998) Site-specific isotope labeling demonstrates a large mesomeric resonance effect of the methoxy groups on the carbonyl frequency in ubiquinones. *Photosynth. Res. 55*, 247−252.
(43) Zwanzig, R. W. (1954) High-temperature equation of state by a perturbation method. I. Nonpolar Gases. *J. Chem. Phys. 22*, 1420−1426.
(44) Rich, P. R., and Harper, R. (1990) Partition coefficients of quinones and hydroquinones and their relation to biochemical reactivity. *FEBS Lett. 269*, 139−144.
(45) Liu, P., Dehez, F., Cai, W., and Chipot, C. (2012) A Toolkit for the Analysis of Free-Energy Perturbation Calculations. *J. Chem. Theory Comput. 8*, 2606−2616.
(46) Bennett, C. H. (1976) Efficient estimation of free energy differences from Monte Carlo data. *J. Comput. Phys. 22*, 245−268.
(47) Hunter, J. D. (2007) Matplotlib: A 2D graphics environment. *Comput. Sci. Eng. 9*, 90−95.
(48) Kirkwood, J. G. (1935) Statistical Mechanics of Fluid Mixtures. *J. Chem. Phys. 3*, 300.
(49) Kollman, P. (1993) Free energy calculations: Applications to chemical and biochemical phenomena. *Chem. Rev. 93*, 2395−2417.
(50) Chipot, C., and Pohorille, A. (2007) *Free Energy Calculations: Theory and Applications in Chemistry and Biology*, Springer, Berlin.
(51) Axelsen, P. H., and Li, D. (1998) Improved convergence in dual-topology free energy calculations through use of harmonic restraints. *J. Comput. Chem. 19*, 1278−1283.

DOI: 10.1021/acs.biochem.5b00033
Biochemistry 2015, 54, 2104−2116

(52) Deng, Y., and Roux, B. (2009) Computations of Standard Binding Free Energies with Molecular Dynamics Simulations. *J. Phys. Chem. B 113*, 2234−2246.
(53) Ellers, P. H. C., and Marx, B. D. (1996) Flexible Smoothing with B-splines and Penalties. *Statistical Science 11*, 89−121.
(54) Steinbrecher, T., Joung, I., and Case, D. A. (2011) Soft-core potentials in thermodynamic integration: Comparing one- and two-step transformations. *J. Comput. Chem. 32*, 3253−3263.
(55) Goldsmith, J. O., and Boxer, S. G. (1996) Rapid isolation of bacterial photosynthetic reaction centers with an engineered poly-histidine tag. *Biochim. Biophys. Acta 1276*, 171−175.
(56) Okamura, M. Y., Isaacson, R. A., and Feher, G. (1975) Primary acceptor in bacterial photosynthesis: Obligatory role of ubiquinone in photoactive reaction centers of *Rhodopseudomonas spheroides*. *Proc. Natl. Acad. Sci. U.S.A. 72*, 3491−3495.
(57) Calvo, R., Abresch, E. C., Bittl, R., Feher, G., Hofbauer, W., Isaacson, R. A., Lubitz, W., Okamura, M. Y., and Paddock, M. L. (2000) EPR Study of the Molecular and Electronic Structure of the Semiquinone Biradical $Q_A^-Q_B^-$ in Photosynthetic Reaction Centers from *Rhodobacter sphaeroides*. *J. Am. Chem. Soc. 122*, 7327−7341.
(58) Utschig, L. M., Greenfield, S. R., Tang, J., Laible, P. D., and Thurnauer, M. C. (1997) Influence of iron-removal procedures on sequential electron transfer in photosynthetic bacterial reaction centers studied by transient EPR spectroscopy. *Biochemistry 36*, 8548−8558.
(59) Shinkarev, V. P., and Wraight, C. A. (1993) in *Photosynthetic Reaction Center* (Deisenhofer, J., and Norris, J. R., Eds.) p 193, Academic Press, San Diego.
(60) Marenich, A. V., Kelly, C. P., Thompson, J. D., Hawkins, G. D., Chambers, C. C., Giesen, D. J., Winget, P., Cramer, C. J., and Truhlar, D. G. (2012) Minnesota Solvation Database 2012.
(61) Garrido, N. M., Economou, I. G., Queimada, A. J., Jorge, M., and Macedo, E. A. (2012) Prediction of the n-hexane/water and 1-octanol/water partition coefficients for environmentally relevant compounds using molecular simulation. *AIChE J. 58*, 1929−1938.
(62) Lyubartsev, A. P., Jacobsson, S. P., Sundholm, G., and Laaksonen, A. (2001) Solubility of Organic Compounds in Water/Octanol Systems. A Expanded Ensemble Molecular Dynamics Simulation Study of log *P* Parameters. *J. Phys. Chem. B 105*, 7775−7782.
(63) Scouras, A. D., and Daggett, V. (2011) The Dynameomics rotamer library: Amino acid side chain conformations and dynamics from comprehensive molecular dynamics simulations in water. *Protein Sci. 20*, 341−352.
(64) Taguchi, A. T., O'Malley, P. J., Wraight, C. A., and Dikanov, S. A. (2014) Nuclear hyperfine and quadrupole tensor characterization of the nitrogen hydrogen bond donors to the semiquinone of the Q_B site in bacterial reaction centers: A combined X- and S-band ^{14,15}N ESEEM and DFT study. *J. Phys. Chem. B 118*, 1501−1509.
(65) Taguchi, A. T., O'Malley, P. J., Wraight, C. A., and Dikanov, S. A. (2014) Hyperfine and nuclear quadrupole tensors of nitrogen donors in the Q_A site of bacterial reaction centers: Correlation of the histidine Nδ tensors with hydrogen bond strength. *J. Phys. Chem. B 118*, 9225−9237.
(66) Stowell, M. H. B., Phillips, T. M., Rees, D. C., Soltis, S. M., Abresch, E., and Feher, G. (1997) Light-induced structural changes in photosynthetic reaction center: Implications for mechanism of electron-proton transfer. *Science 276*, 812−816.
(67) Flores, M., Isaacson, R., Abresch, E., Calvo, R., Lubitz, W., and Feher, G. (2007) Protein-cofactor interactions in bacterial reaction centers from *Rhodobacter sphaeroides* R-26: II. Geometry of the hydrogen bonds to the primary quinone Q_A^- by ^{1}H and ^{2}H ENDOR spectroscopy. *Biophys. J. 92*, 671−682.
(68) Martin, E., Samoilova, R. I., Narasimhulu, K. V., Wraight, C. A., and Dikanov, S. A. (2010) Hydrogen bonds between nitrogen donors and the semiquinone in the Q_B site of bacterial reaction centers. *J. Am. Chem. Soc. 132*, 11671−11677.
(69) Martin, E., Samoilova, R. I., Narasimhulu, K. V., Lin, T.-J., O'Malley, P. J., Wraight, C. A., and Dikanov, S. A. (2011) Hydrogen bonding and spin density distribution in the Q_B semiquinone of bacterial reaction centers and comparison with the Q_A site. *J. Am. Chem. Soc. 133*, 5525−5537.
(70) Zhao, N., and Hastings, G. (2013) On the nature of the hydrogen bonds to neutral ubiquinone in the Q_A binding site in purple bacterial photosynthetic reaction centers. *J. Phys. Chem. B 117*, 8705−8713.
(71) Sinnecker, S., Flores, M., and Lubitz, W. (2006) Protein-cofactor interactions in bacterial reaction centers from *Rhodobacter sphaeroides* R-26: Effect of hydrogen bonding on the electronic and geometric structure of the primary quinone. A density functional theory study. *Phys. Chem. Chem. Phys. 8*, 5659−5670.
(72) Paddock, M. L., Flores, M., Isaacson, R., Chang, C., Abresch, E. C., and Okamura, M. Y. (2007) ENDOR Spectroscopy Reveals a Light Induced Movement of the H-Bond from Ser-L223 Upon Forming the Semiquinone (Q_B) in Reaction Centers from *Rhodobacter sphaeroides*. *Biochemistry 46*, 8234−8243.
(73) Ishikita, H., and Knapp, E.-W. (2004) Variation of Ser-L223 hydrogen bonding with the Q_B redox state in reaction centers from *Rhodobacter sphaeroides*. *J. Am. Chem. Soc. 126*, 8059−8064.
(74) Zhu, Z., and Gunner, M. R. (2005) Energetics of quinone-dependent electron and proton transfers in *Rhodobacter sphaeroides* photosynthetic reaction centers. *Biochemistry 44*, 82−96.
(75) Martin, E., Baldansuren, A., Lin, T.-J., Samoilova, R. I., Wraight, C. A., Dikanov, S. A., and O'Malley, P. J. (2012) Hydrogen bonding between the Q_B site ubisemiquinone and Ser-L223 in the bacterial reaction center: A combined spectroscopic and computational perspective. *Biochemistry 51*, 9086−9093.
(76) Alexov, E. G., and Gunner, M. R. (1999) Calculated protein and proton motions coupled to electron transfer: Electron transfer from Q_A^- to Q_B in bacterial photosynthetic reaction centers. *Biochemistry 38*, 8253−8270.
(77) Mavelli, F., Trotta, M., Ciriaco, F., Agostiano, A., Giotta, L., Italiano, F., and Milano, F. (2014) The binding of quinone to the photosynthetic reaction centers: Kinetics and thermodynamics of reactions occurring at the Q_B-site in zwitterionic and anionic liposomes. *Eur. Biophys. J. 43*, 301−315.

DOI: 10.1021/acs.biochem.5b00033
Biochemistry 2015, 54, 2104−2116